COMMISSIONING RESULTS OF THE LCLS INJECTOR*

D. H. Dowell#, R. Akre, Y. Ding, P. Emma, J. Frisch, S. Gilevich, G. Hays, Ph. Hering, Z. Huang,
R. Iverson, C. Limborg-Deprey, H. Loos, A. Miahnahri, J. Schmerge, J. Turner, J. Welch,
W. White, J. Wu, *SLAC, Stanford*, CA 94309, USA,
L. Froelich, T. Limberg, E. Prat, *DESY, Hamburg*, Germany

Abstract

The Linac Coherent Light Source (*LCLS*) is a SASE x-ray Free-Electron Laser (FEL) project presently under construction at SLAC [1]. The injector section, from drive-laser and RF photocathode gun through first bunch compressor chicane, was installed in fall 2006. Initial system commissioning with an electron beam has recently been completed. The second phase of construction, including second bunch compressor and full linac, is planned for 2008. In this paper, we report experimental results and experience gained during the first phase of machine commissioning. This includes the cathode, drive laser, RF photocathode gun, linac booster section, S-band and X-band RF systems, first bunch compressor, and the various beam diagnostics.

INTRODUCTION

The months of April through August 2007 have been spent commissioning the *LCLS* injector. This is the first phase of machine commissioning, with the second phase starting in Dec. 2007 after a 3-month downtime, and the final phase in Nov. 2008, culminating in FEL light in 2009. First electrons from the new photocathode RF gun were observed on April 5 and beam was quickly established to the full (injector) energy of 250 MeV in the main SLAC linac on April 14, 2007 [2]. Over the next five months all the injector systems were commissioned and the beam accelerated to 15 GeV at the end of the SLAC linac. The bunch charge (1 nC) and the measured projected emittance of 1.2 microns meets the design requirements of LCLS.

DESCRIPTION OF THE INJECTOR

Figure 1 shows the major components of the LCLS injector at the 2 kilometer point of the 3 kilometer SLAC linac. The off-axis housing was built during the original construction of the linac in 1962 [3], anticipating future injection beamlines such as LCLS.
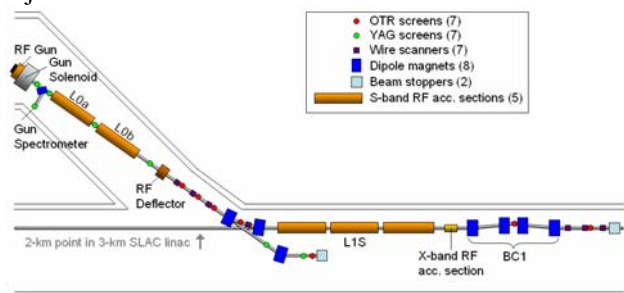

Figure 1: The injector for LCLS located in the off-axis housing at Sector 20, at the 2/3-point along the linac.

The LCLS injector begins with a photocathode RF gun followed by two modified SLAC linac sections producing a beam at 135 MeV, 100 amps peak current and transverse normalized emittance of 1.2 microns for 1 nC bunches. The cathode drive laser is located in a reconstructed alcove above the RF gun. The 135-MeV beam is deflected onto the main linac axis by a two-dipole 35 degree doubly achromatic bend or, with the first 17.5 degree dipole magnet turned off, the beam drifts to a 35 degree straight ahead spectrometer for energy and energy spread measurements. Once on the axis of the main linac, the electrons are accelerated to 250 MeV in three linac structures before entering the first chicane bunch compressor, BC1. Between the three linacs and BC1 is a short x-band structure whose 4th harmonic straightens the beam's longitudinal phase space for linear compression.

THE DRIVE LASER

The RF gun's copper cathode is illuminated by a UV laser operating at 255 nm delivering up to 450 microjoules per pulse at 120 Hz. In addition to the wavelength and energy, the laser must meet stringent stability and reliability requirements as well as strict transverse and longitudinal shaping specifications. The stability specifications were achieved with a pulsed Ti:sapphire system pumped by two quasi-cw, diode pumped Nd:YAG lasers (Figure 2); however the shaping requirements have not been met.
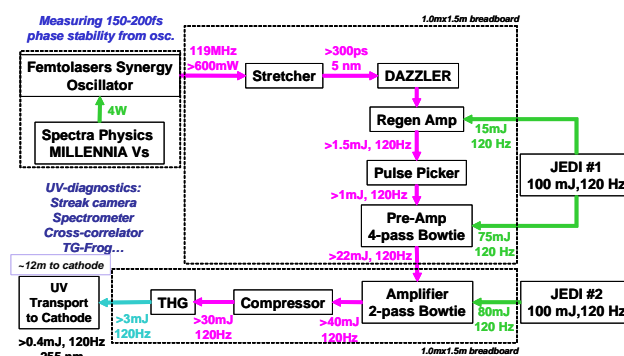

Figure 2: A block diagram of the RF gun drive laser designed and built by Thales Lasers.

The laser pulse shape is measured by combining a short pulse from the oscillator with the UV pulse in a non-linear crystal allowing back-conversion of the mixed signal to the second harmonic. A cross correlation measurement of the UV pulse sent to the cathode is shown in Figure 3.
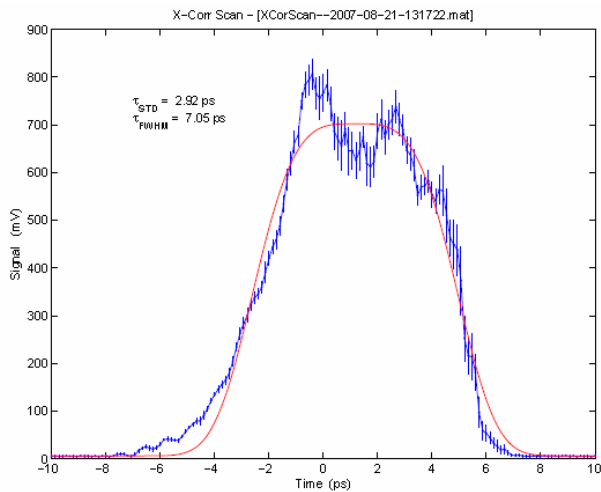
Figure 3: The laser pulse shape as measured in a cross correlator and fit with an n-order super Gaussian.

The short-term charge stability which results both from the laser's energy and the laser-RF phase jitter is shown for a measurement period of 53 seconds in Figure 4. The charge was determined with a beam position monitor (BPM) located immediately after the gun and demonstrates 1.1% (rms) charge stability, which easily meets the 2% specification for stable operation of the LCLS FEL. The long-term variation is controlled using a feedback loop which varies the laser energy using an adjustable wave-plate inside the IR to UV tripler.
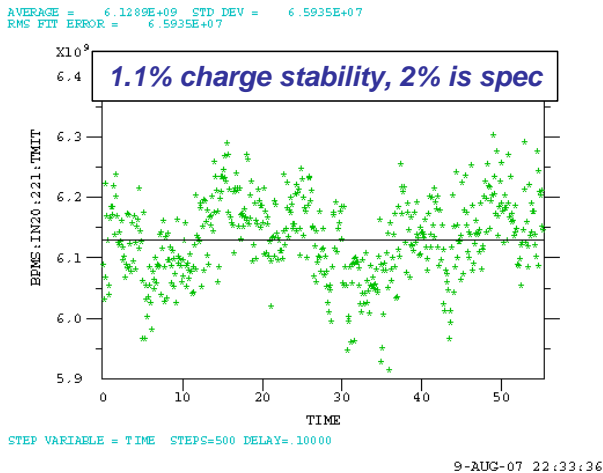

Figure 4: The laser's short-term energy stability of 1.1% (rms) is better than the design specification of 2%.

The laser transverse profile is monitored on the virtual cathode camera (VCC) which views the light from a beam splitter located just before the UV beam enters the beamline vacuum. Figure 5 shows a typical VCC image which is used in a feedback loop with a steering mirror to maintain the laser beam at a fixed point on the cathode. The details of this optical system have been described in ref [4].
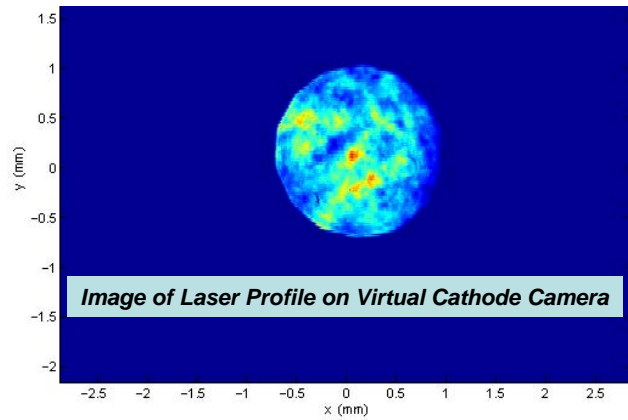

Figure 5: A typical image of the laser transverse profile on the virtual cathode camera.

THE PHOTOCATHODE RF GUN

The LCLS photocathode RF gun has been described elsewhere [5,6] and only its general features are summarized here. The gun fields are fully rotationally symmetric by incorporating dual feed (to eliminate the dipole fields) and a racetrack geometry (to cancel the quadrupole fields induced by the dual feed) for the full cell into which the RF is coupled.

Since this gun is the sole electron source for the LCLS user facility, it needs to operate reliably at the relatively high repetition rate of 120 Hz as well as producing exceptional quality beam. This was done by making several changes to the BNL/SLAC/UCLA gun.

The LCLS gun was made more reliable by replacing the commonly used azimuth angle RF coupling with much larger z-coupled ports running the full length of the full cell. This approach combined with careful design of the coupler-hole lip radii greatly reduced the pulsed heating which otherwise would have limited the gun lifetime. In addition, any field emission from the tuning slugs was eliminated with deformation tuners. These tuners where found to be unnecessary during the tuning process. In addition, the shape of the iris between the two cells was modified to reduce its surface fields below that of the cathode. The resulting cathode surface field is approximately 10% higher than the iris fields. With these modifications the gun was easily conditioned to 120 MV/m and 60 Hz repetition rate. Conditioning at 120 Hz was limited to 107 MV/m due to excessive heating of the gun probes, a limitation which will be corrected by the installation of re-designed probes in 2008. Therefore to reduce any risk of damaging the gun, it was decided to limit the repetition rate to 30 Hz during the 2007 commissioning run. As a result, the gun operated continuously at 30 Hz for more than 3×10^8 pulses during the April 5, 2007 to August 24, 2007 commissioning period.

Another important innovation of the gun which improved its beam quality was to greatly increase the frequency separation of the 0- and pi-modes. Previous s-band guns had been built with 3.2 MHz separation resulting in excitation of the undesired 0-mode by the low

frequency components of RF envelope waveform, allowing it to beat against the pi-mode. The presence of the 0-mode increases the correlated energy spread and unbalances the fields between the two cells both during transient and in steady state [5,6]. Increasing the mode separation to 15 MHz greatly reduces excitation of the 0-mode, giving a pure pi-mode in the gun.

THE CATHODE

The cathode quantum efficiency was quite low for the first two months of commissioning. To complicate the issue, the QE had the appearance of being even lower due to incorrect Faraday cup measurements. Once the beam was transported to the main linac, its charge was more accurately measured using known SLAC-standard charge and beam position monitors. However this correction was only a factor of 1.45, while the QE was initially almost 20-times lower than the design requirement.

In order to understand the poor cathode performance, the cathode was imaged optically with white light and a camera in reflection geometry, and the emission distribution imaged with the gun solenoid adjusted to create a point-to-point image of the cathode photo-emission on the second YAG screen [7]. Illumination for the white light image was done by directing light through the UV optics and vacuum window, and reflecting light off the in-vacuum mirror onto the cathode. A digital camera viewed the cathode with the opposing in-vacuum mirror (installed for wakefield compensation) and vacuum window. The photo-emission imaging was done at approximately 10pC bunch charge in order to minimize space charge forces blurring of the image. A comparison of these two methods of imaging is shown in Figure 6. The resolution with both techniques is excellent and the correspondence between the white light features and the areas of high photo-emission is striking.
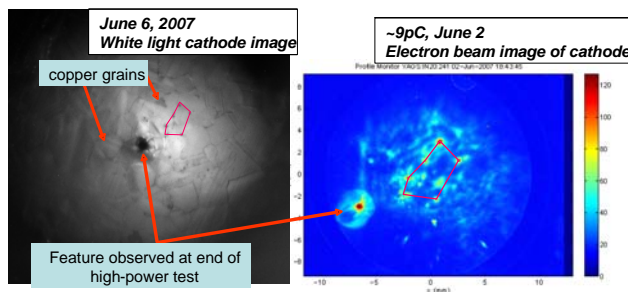

Figure 6: Images of the cathode taken using a white light source and a camera (left), and an electron emission image on a YAG screen approximately 100 cm from the cathode. The gun solenoid is adjusted to image the cathode electrons on the 100 micron thick YAG screen.

The initial QE at the start of commissioning was approximately 2 to 3 x 10^{-6} which is 20-times lower than the design specification of 6 x 10^{-5}. This very low QE limited the maximum beam charge to 200pC during the first half of commissioning. However, reducing the laser size on the cathode during the emittance studies increased

the laser fluence to the degree that vacuum activity in the form of low-level RF arcs were observed which cleaned the cathode. The result has been a fortuitous, steady rise in QE during the last three months of commissioning as can be seen in Figure 7.
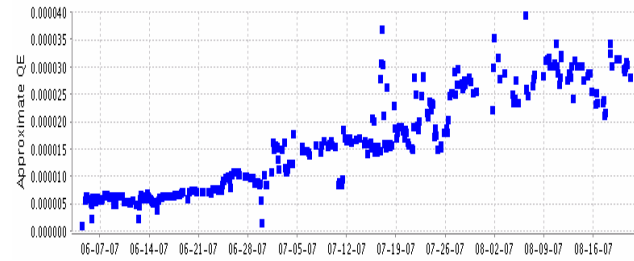

Figure 7: The quantum efficiency during the last two and one-half months of commissioning.

A mild laser cleaning of the cathode was also performed. The fluence was deliberately kept low and only one pass of the scan was done to limit any possible damage to the cathode surface. The QE before and after cleaning is shown in Figure 8, which was done in the presence of low rf power of 1 MV rather than the nominal 6MV, equivalent beam energy. The laser-RF phase was also nominal at 30 degS from the zero crossing. The laser fluence was approximately 360 microjoules per sq. mm in a 0.67 mm diameter laser spot slowly moved over a 2 mm x 2 mm area. The dwell time was 10 seconds at each position with a 100 micron step size. The initial and final QE's were 1.6x10^{-5} and 2.8x10^{-5}, respectively.
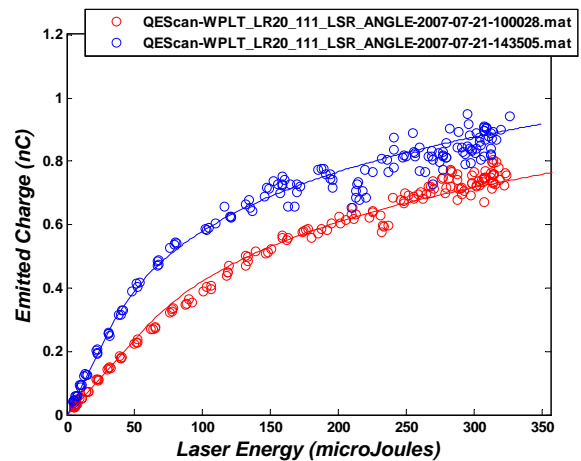

Figure 8: The measured charge vs. laser energy before (red) and after (blue) laser cleaning.

The QE history shown in Figure 7 is an approximation based upon the charge emitted at the RF phase producing the maximum cathode field (approximately 90 degS from the zero field phase), normalized to the laser energy. A more precise measurement is given in Figure 9 where the charge is given as a function of the laser energy at the laser-RF phase of 30 degS from the RF zero crossing. The linear portion at low laser energies gives the quantum efficiency and the onset of the space charge limit is

indicated by the roll-over of the curve from this linear dependence. The space charge limit is quantified by an effective transverse rms radius assuming a Gaussian distribution [8,9]. The inserted image in Figure 9 shows the actual transverse emission distribution as imaged on the YAG screen as described above. This image corresponds to the laser iris completely opened while the charge vs. laser energy data was taken with the iris set to a 1.3 mm diameter cathode illumination.
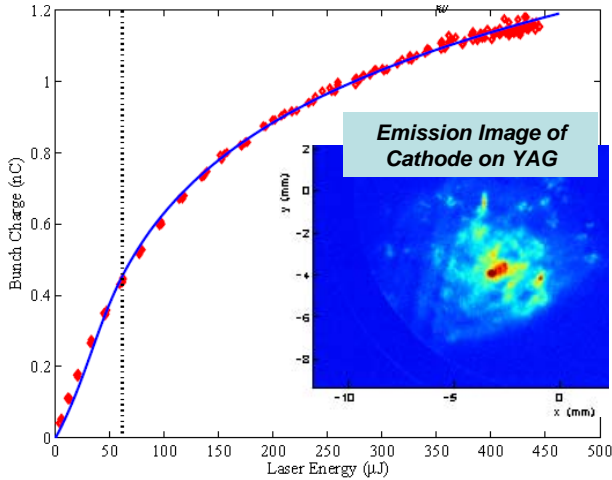

Figure 9: The measured bunch charge vs. laser energy fit with an analysis for the QE and the space charge limit. The QE in this case was 3.7×10^{-5} and the effective transverse radius 0.34 mm (rms). The inset shows the emission distribution with the laser iris fully open when this data was taken. The scale corresponds to the beam size on the YAG screen.

MEASUREMENT AND ANALYSIS OF THE TRANSVERSE EMITTANCE

The LCLS injector transverse emittance at 135 MV is measured using optical transition radiation (OTR) with a 1-micron thick aluminum foil. The images are acquired with a digital camera, background subtracted and analyzed using a variety of methods to eliminate spurious results due to long tails of the distribution. The on-line software allows x- and y-plane projections of the images to be analyzed for rms beam size based on several methods, including: 1) rms of the entire profile, 2) Gaussian fit, 3) asymmetric Gaussian fit, 4) 5% amplitude cut, and 5) 5% area (charge) cut.

The results reported here use the 5% area cut technique. In this method the background subtracted image is integrated in the two transverse dimensions over the region of interest (ROI) and the threshold level corresponding to 5% of the area-integrated image is found. The rms beam sizes for the projections above this threshold are used to compute the emittance.

The emittance results using the 5% area cut analysis are given in Figure 10. The plots on the left show the rms beam size as a function of the quadrupole field with fitted curve overlaid. The beam emittance, Twiss and matching parameters, as well as the goodness of fit are listed on the

plot. The ellipses on the right represent the reference phase space of the x- and y-planes at the OTR screen location for the nominal quadrupole field. The straight lines represent the beam size at each quadrupole setting, transformed to the reference phase space.
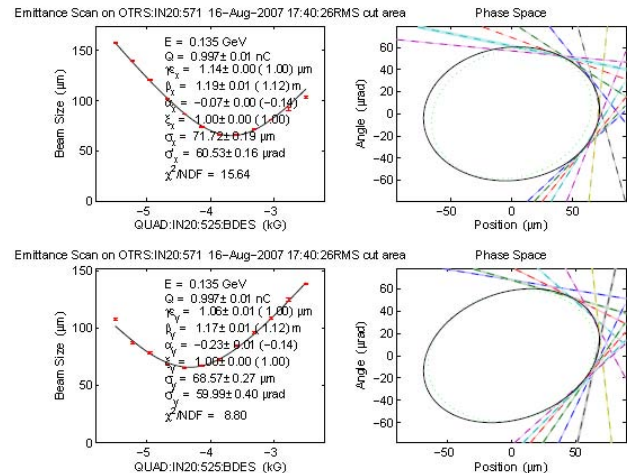

Figure 10: Projected normalized emittance measured for a 1 nC bunch at 135 MeV ($\gamma \varepsilon_x = 1.14 \, \mu m$, $\gamma \varepsilon_y = 1.06 \, \mu m$).

The electron bunch slice emittance is measured on the same OTR screen with the transverse RF deflector switched on, applying the same 5% area cut analysis method to the data. A typical image with the deflector switched on is shown in the center image of Figure 13. In Figure 11, the bunch has been binned into 12 slices and the horizontal emittance calculated for each slice.
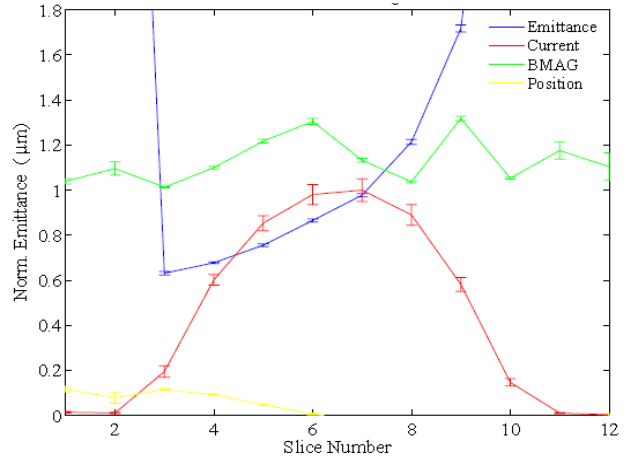

Figure 11: The slice horizontal emittance for a 1-nC, 100-ampere bunch at 135 MeV, with emittance values <1 μm in the beam core.

Simulations of the beam emittance measurement were performed using the IMPACT particle tracking code [10]. In these calculations the electron emission images shown in Figures 6 and 9 and the laser pulse shape given by the cross correlator were used for the starting particle distributions at the cathode surface. Therefore both the transverse and longitudinal asymmetries associated with the initial conditions were included in the simulation. This realistic electron beam distribution was accelerated to 135 MeV and propagated to the OTR screen to

simulate the quadrupole scan technique. The computed transverse profiles were analyzed with the same area cut method as done in the experiment to obtain the emittance as a function of the area cut percentage.

The result of this analysis is summarized in Figure 12 where the transverse emittances are plotted as functions of the percentage of area cut. The higher y-plane emittance results from the asymmetry of the initial electron distribution and is typical of the emittance asymmetry observed in the measurements.

Comparing the measured emittances of Figure 10 with the curves in Figure 12, indicate that a percentage cut of 8 to 9% would result in good agreement with simulation. Whereas the measurement technique described above used 5% for the cut area, it is possible that a few per cent of the measured distribution is lost in the camera noise or there is a subtle difference between the measured and simulated tails at the level of a few percent. In any case, this discrepancy is relatively small, and at worse would imply the measured emittances are for 90 to 93% of the beam charge rather than 95%.
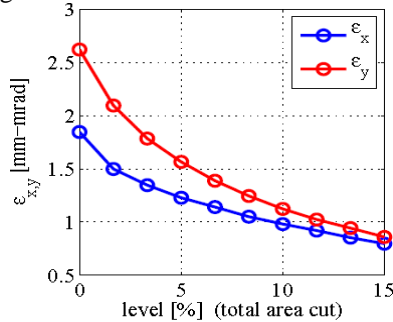

Figure 12: Simulations of the emittance as a function of the percentage area of the tails cut from the data.

BUNCH LENGTH COMPRESSION

The LCLS injector includes a 4-dipole magnetic chicane (BC1) at 250 MeV as the first bunch compression stage. (The second compressor, BC2, will be located 350 m downstream at 4.3 GeV and installed in fall 2007.) Nominally, the bunch is compressed by a factor of 4-5 in BC1, but in the extreme, with X-band 4th harmonic RF switched 'ON' to linearize the energy chirp (see Fig. 15), the bunch can be compressed down to a few microns [11]. The chicane includes an OTR screen, adjustable collimator, and a BPM at its center.
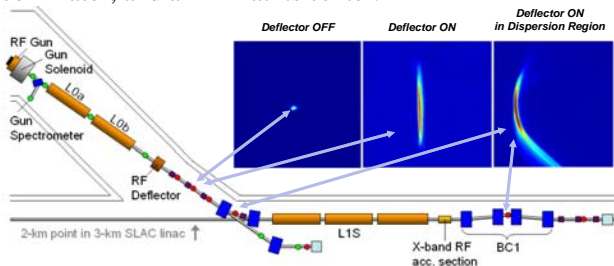

Figure 13: OTR foil images with 1st RF-deflector cavity 'OFF' (left), then cavity 'ON' to measure slice emittance (center), and again 'ON' with an OTR foil at high dispersion to measure longitudinal phase space (right).

The absolute bunch length after BC1 has been measured using a 2.4-m long vertical RF deflecting cavity (LOLA) 900 m downstream of BC1, which acts as a streak camera [11]. The bunch length measurements are shown in Fig. 14 at 1 nC, where the energy spread induced by the off-crest phase of the L1S and X-band RF sections (see Fig. 2) is varied, producing the rms relative energy spread on the horizontal axis of this plot. The compression factor was also measured simultaneously by using two beam phase monitor cavities, one up and one downstream of BC1, to measure the ratio of phase variations at each location as the phase of the drive laser is scanned. This compression factor is multiplied by the measured initial bunch length and plotted for easy comparison with the measured bunch length data. This measurement is presently resolution limited by a phosphor screen, which will be replaced during the fall 2007 installation period with a new OTR foil at 4.3 GeV. The poor agreement of the data in the range $\sigma_E/E > 4\%$ may be due to coherent synchrotron radiation in the compressor.
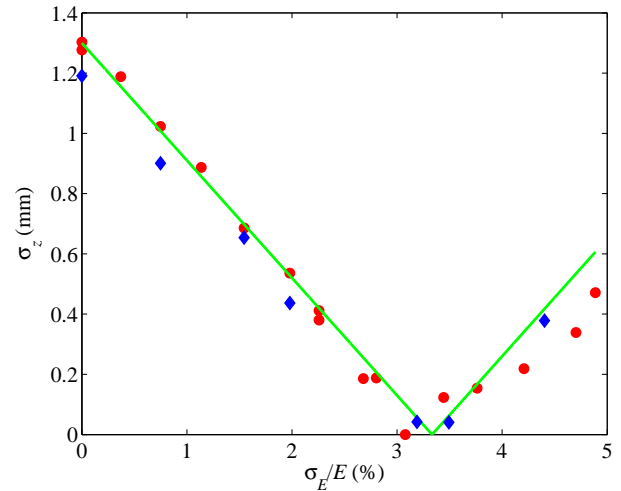

Figure 14: Bunch length after BC1 measured using the RF deflector (red-circles), and initial bunch length times compression factor (blue-diamonds) measured using two beam phase monitor cavities up and downstream of BC1. The calculated bunch length is also shown (green line).

The 2.4-m LOLA cavity will be relocated closer to the BC2 in fall '07, but is presently near the linac end at 14 GeV. A shorter transverse cavity is also located upstream of BC1 (Figs. 1 and 13) and used to measure the initial bunch length and longitudinal distribution (Fig. 16, left). The 14-GeV bunch was also compressed to 170 micron rms bunch length (Fig. 16, right), and smaller, but with a resolution limit of about 100 μm rms, which will be upgraded in 2007 with a new OTR foil at 4.3 GeV.

The BC1 dipole fields are unfortunately of poor quality, including a significant sextupole field and linear field gradient, which generates large horizontal dispersion and emittance growth beyond BC1. The linear dispersion has been corrected using two small quadrupoles placed in BC1 for this purpose, but the sextupole field limits the minimum horizontal emittance growth to about 40% ($\gamma\varepsilon_x$

from 1.2 μm before BC1 up to 1.7 μm after BC1). The dipole magnets will be re-worked in the fall of 2007.
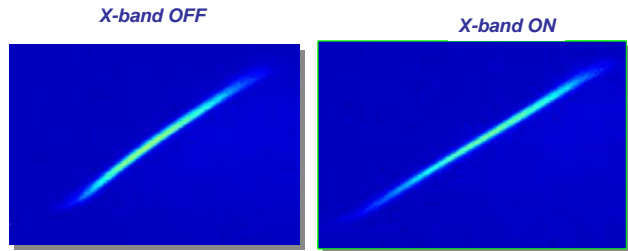

Figure 15: OTR screen in BC1 chicane with its horizontal dispersion. The first RF deflector is 'ON' here, with the X-band cavity 'OFF" at left, and 'ON' at right, demonstrating linearization of the energy chirp.
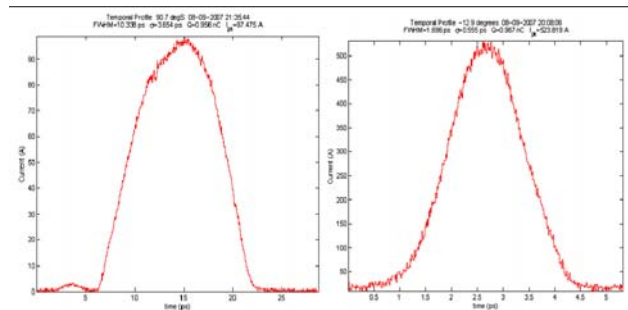

Figure 16: Bunch length distribution measured using both RF deflectors. The first measurement is at 135 MeV (left, $\sigma_z \approx 1.1$ mm, $I_{pk} \approx 97$ A) and the second is at 14 GeV (right, $\sigma_z \approx 0.17$ mm, $I_{pk} \approx 520$ A), representing the bunch length before and after BC1 compression at 1 nC.

BC1 BUNCH LENGTH MONITORS

The bunch length is monitored after BC1 using two techniques. One, referred to as BL12, incorporates a ceramic gap incorporated into the beam pipe downstream of the compressor. The microwave radiation generated by the short bunch's wakefields is transmitted through the ceramic and is detected by two fast, microwave detectors which are sensitive to 100 and 300 GHz. Once calibrated against the bunch length measurements using the LOLA transverse deflecting cavity, these signals are used to feedback the L1S RF phase and regulate the bunch length.

Another bunch length monitor located immediately after the last BC1 dipole measures the coherent synchrotron radiation, edge radiation and diffraction radiation generated by the short bunch as it passes through the dipole and a holed mirror. A collection lens images the edge radiation onto a pyroelectric detector. The general layout is given schematically in Figure 17.
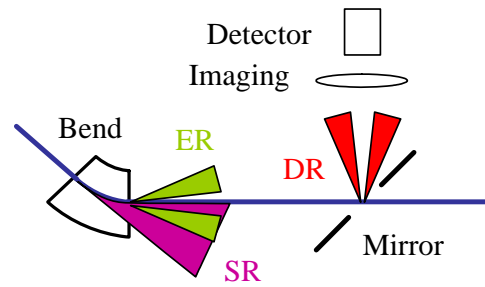

Figure 17: The radiation sources viewed by bunch length monitor, BL11. The pyroelectric detector measures the combined sources of synchrotron radiation (SR), edge radiation (ER) and diffraction radiation (DR) reflected into the detector by a mirror with a hole through which the electron beam passes.

Further details of the BL11 bunch length monitor are shown in Figure 18. The system splits the radiation into two detectors each of which has two high-pass filters at 0.5 mm and 1.0mm which can be inserted for selecting the wavelengths of interest. The responses of these detectors for the cases of no filter, and with the 0.5 mm and 1.0 mm filters inserted as functions of the L1S phase are plotted in Figure 19. Increasing L1S accelerator phase increases the bunch energy chirp resulting in stronger compression in BC1.
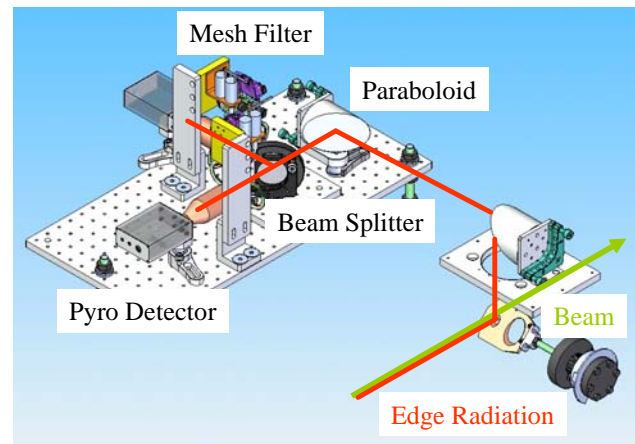

Figure 18: A computer generated drawing of the BL11 bunch length monitor system.
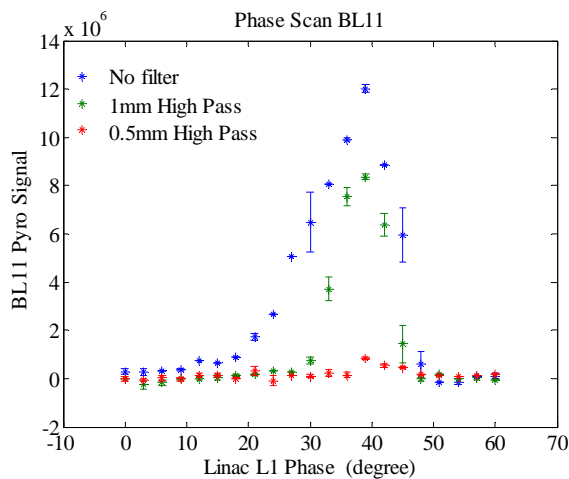
Figure 19: The response of the pyroelectric detector as a function of the phase of the linac section before the bunch compressor. The signal is given for no wavelength filter, a 1mm high pass filter and a 0.5mm high pass filter.

UNEXPECTED PHYSICS

During the beam emittance studies after BC1, we began observing a strong enhancement of the optical signal from the OTR foils when the bunch was highly compressed. The effect is illustrated in Figure 20 where the BL12 microwave detector signals and the OTR optical signal obtained by integrating OTR image are given vs. the L1S RF phase in a semi-log plot. Recall that increasing the L1S phase, decreases the electron bunch length where the L1S phase for nominal LCLS operation is 25 degS. The data show expected behavior for the two microwave signals. The lower frequency 100 GHz signal is first to respond, followed by the 300 GHz detector near 35 degS. The 300 GHz signal saturates above 40 degS.

What is unexpected is the large increase in the OTR optical signal, rising at least an order of magnitude above the unbunched signal. This behavior of the optical signal strength suggests there is micro-bunching of the electron beam at optical wavelengths.

In addition to this large increase in the optical signal, the beam image greatly varies from pulse to pulse. This can be seen in the large error bars at high-compression phases shown in Figure 20, which reflect the large shot-to-shot variation. Similar variations are seen in the profile projections given in Figure 21 for a sequence of beam pulses. The images themselves are similarly striking, displaying chaotic patterns of random spots which can be organized into a ring-like shape with the proper settings of the upstream quadrupoles. This fascinating effect can be seen in Figure 22. And again, these phenomena indicate the generation of coherent optical radiation due to micro-bunch instability.

Another indication of this interesting phenomenon is shown in Figure 23. In this study, the OTR optical signal for the foil is shown, but in this case, BC1 is articulated to zero degrees so as to have zero R_{56}. The quadrupole singlet between the two 17.5 degree dipoles of DL1 (see Fig. 1) is varied and the optical intensity is found to vary

with a Gaussian shape, centered exactly at the setting which makes the DL1 dipole-quadrupole-dipole bend doubly achromatic.
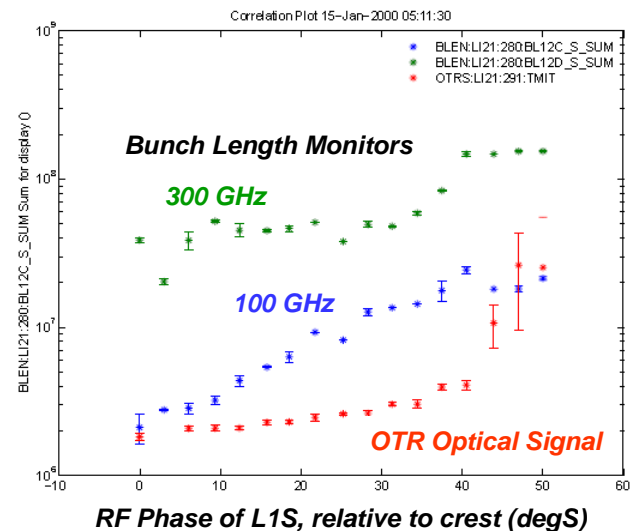

Figure 20: The signals of the BL12 microwave detectors at 100 (blue) and 300 (green) GHz, and the image-integrated OTR optical signal (red) as seen by a digital camera are plotted as functions of the L1S phase relative the crest.
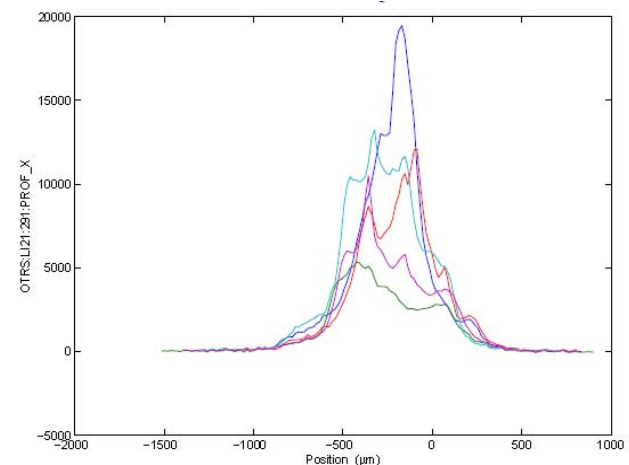

Figure 21: Profile projections for five consecutive beam pulses when the RF phase is set at 50 degS.

The data in Figure 22 can be explained by assuming the bunch has an energy modulation on the scale of optical wavelengths before entering DL1. This modulation is converted to current modulation by the 4 mm R_{56} of DL1 which then coherently radiates transition radiation at the OTR foil. Varying the quadrupole from its design field not only makes the bend dispersive but also results in non-zero values for the R_{51} and R_{52} matrix elements which can mix the bunches by tilting them in the transverse direction, smearing the current modulation and reducing the COTR signal. The coherent optical radiation (COTR) is the strongest when the quadrupole is set for DL1 achromatic with R_{51} and R_{52} equal to zero. A possible source of the initial energy modulation is shot-noise, as the drive laser doesn't have enough bandwidth to produce

such optical scale modulations. Experimental and theoretical investigations are in progress.
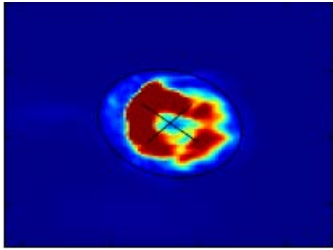

Figure 22: An image of the COTR radiation obtained by careful adjustment of the quadrupoles after the bunch compressor.
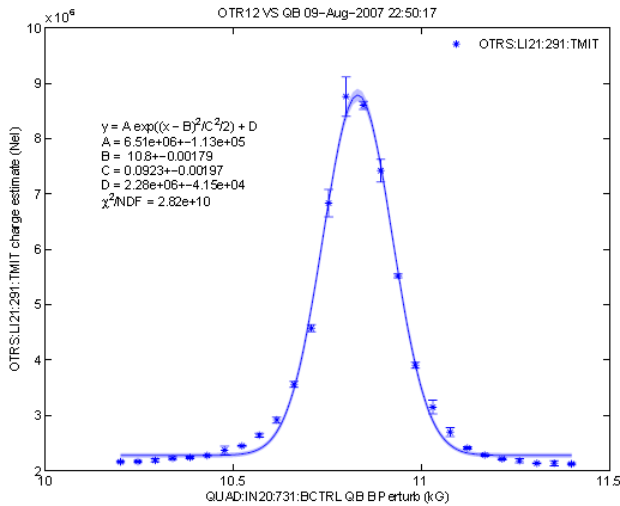

Figure 23: The integrated optical transition radiation signal as a function of the quadrupole single between the 17.5 degree bends. The optical signal is a maximum at the quadrupole setting which makes the DL1 bend doubly achromatic.

SUMMARY AND DISCUSSION

The design and beam properties measured during the five month commissioning run are listed in Table I. These results unambiguously show the injector meets all the beam requirements for the LCLS.

The five month commissioning period not only successfully validated the injector design and its operation, but also observed strong coherent effects in the beam diagnostics and transport on the optical scale. These effects are yet another indication of excellent beam brightness, and show we are now entering a new era of beam physics where coherence dominates not only with the FEL interaction, but also during the production, acceleration, transport and manipulation of these dense electron bunches. The LCLS injector commissioning additionally makes it clear that coherence and interference effects will play a major role in future beam diagnostics. Hence LCLS ushers in a new era not only of [4th] generation light sources, but also of bright electron beams which coherently radiate all too easily.

Table I: The design and measured beam properties.

Parameter	sym	dsgn	meas.	unit
Final e^- energy	γmc^2	14	14	GeV
Bunch charge	Q	1	1	nC
Init. bunch length (fwhm)	Δt_0	10	10	ps
Fin. bunch length (fwhm)	Δt_f	2.3	1.5-10	ps
Initial peak current	I_{pk0}	100	100	A
Projected norm emittance	$\gamma\varepsilon_{x,y}$	1.2	1.1 - 1.2	μm
Slice norm. emittance	$\gamma\varepsilon^s_{x,y}$	1.0	0.7 - 1.0	μm
Single bunch rep. rate	f	120	10-30	Hz
RF gun field at cathode	E_g	120	115	MV/m
Laser energy on cathode	u_l	250	300	μJ
Laser wavelength	λ_l	255	255	nm
Laser diameter on cath.	$2R$	1.5	1.3	mm
Cathode material	-	Cu	Cu	
Cathode quantum eff.	QE	6	3.5	10^{-5}
Commissioning duration	-	8	5	mo

REFERENCES

[1] J. Arthur *et al.*, SLAC-R-593, April 2002.

[2] R. Akre, *et al.*, PAC'07, Albuquerque, NM, 2007.

[3] "The Stanford Two-Mile Accelerator," R. B Neal, Ed., W. A. Benjamin 1968, pp.1123-1124. http://www.slac.stanford.edu/spires/hep/HEPPDF/twomile/Stanford_Two_Mile_Complete.pdf

[4] D. H. Dowell, J. Castro, P. Emma, J. Frisch, S.Gilevich, G. Hays, P. Hering, C. Limborg-Deprey, H. Loos, A. Miahnahri and W. White, "LCLS Injector Drive Laser," PAC'07, Albuquerque, NM, 2007.

[5] C. Limborg-Deprey, D. Dowell, J. Schmerge, Z. Li and L. Xiao, "RF Design of the LCLS Gun" LCLS-TN-05-3, Feb. 2005.

[6] L. Xiao, R.F. Boyce, D.H. Dowell, Z. Li, C. Limborg-Deprey, and J.F. Schmerge, "Dual Feed RF Gun Design for the LCLS", SLAC-PUB-11213 and PAC'05, Knoxville, TN, 2005.

[7] D.H. Dowell, E. Jongewaard, C. Limborg-Deprey, J. Schmerge and A. Vlieks, "Measurement and Analysis of Field Emission Electrons in the LCLS Gun," PAC'07, Albuquerque, NM, 2007.

[8] J. Rosenzweig *et al.*, "Initial Measurements of the UCLA RF PhotoInjector", NIM A 341 (1994) 379-385.

[9] J. L. Adamski *et al.*, "Results of commissioning the injector and construction progress of the Boeing one kilowatt free-electron laser", SPIE Vol. 2988, p158-169.

[10] C. Limborg-Deprey, D. H. Dowell, P. Emma, R. Iverson, J. Frisch, H. Loos, J. Turner, J. Schmerge, J. Welch, J .Wu, Y. Ding, Z. Huang, J. Castro, G. Hays, P. Hering, S. Gilevich, A. Miahnahri and W. White, "Simulations for the LCLS Injector," These Proceedings.

[11] P. Emma *et al.*, PAC'07, Albuquerque, NM, 2007.

[12] R. Akre *et al.*, PAC'01, Chicago, IL, June 2001.